Macromolecules
ARTICLE

Macromolecules **2010**, *43*, 8121–8127 **8121**
DOI: 10.1021/ma101615k

Characterization by Atomic Force Microscopy of the Nanoheterogeneities Produced by the Radiation-Induced Cross-Linking Polymerization of Aromatic Diacrylates

Mickael Krzeminski,[†] Michael Molinari,[‡] Michel Troyon,[‡] and Xavier Coqueret*[,†]

[†]*Université de Reims Champagne-Ardenne, Institut de Chimie Moléculaire de Reims CNRS UMR 6229, Moulin de la Housse, BP 1039, 51687 Reims Cedex 2, France, and* [‡]*Laboratoire de Microscopies et d'Etude de Nanostructures, LMEN EA3799, 21 rue Clement Ader, 51685 Reims Cedex 2, France*

Received July 18, 2010; Revised Manuscript Received August 31, 2010

ABSTRACT: Atomic force microscopy was used in the tapping mode for studying the heterogeneities in radiation-cured acrylate networks via phase imaging of local viscoelasticity. Film samples were prepared by UV- or electron beam-initiated polymerization of a bisphenol-A-derived ethoxydiacrylate or of the epoxydiacrylate analogue under nitrogen. The top surface of the samples, nearly flat at the atomic level, was probed under moderate to hard tapping conditions. The phase images revealed the heterogeneous character of the network that can be interpreted in terms of local variations of cross-link densities. Appropriate image treatment was applied to determine a set of geometric descriptors for samples exhibiting monomer conversion levels ranging from 0.3 to 0.8. Rigid nodules exhibiting a mean characteristic dimension of ~15 nm were observed very early in the cross-linking polymerization process. Those clusters initially embedded in a soft gel undergo limited evolution by growth and by aggregation up to a limiting size at higher conversion levels. Nucleation within the monomer-rich domains further continues up to ca. 50% conversion, together with limited growth by aggregation of adjacent particles. Polymerization then continues in interstitial domains, generating a stringy network with some isolated low conversion domains. These different features were observed for both aromatic diacrylate monomers and were qualitatively similar in EB- and UV-cured samples, without significant influence of the initiation mechanism and initiation rate on the nanostructure of the studied networks.

Introduction

Radiation-induced cross-linking polymerization produces highly cross-linked, heterogeneous networks[1] as a result of a complex chain-growth mechanism and chain kinetics[2,3] that have been studied for several decades.[4] During the last years, the development of finer experimental methods has made it possible to study more deeply the structural features of networks obtained by radiation-induced free radical processes. A general agreement for the description of the resulting material consists of a juxtaposition of highly cross-linked particles interconnected by continuous domains made of a weakly cross-linked polymer phase gradually driven to the glassy state.[5,6]

During the last 20 years, following the original discussion on microheterogeneity in multiacrylate systems by Kloosterboer,[7] several authors have investigated heterogeneity issues by various experimental techniques[8,9] and by simulation of network build-up.[10,11] However, a relevant qualitative description of the overall hardening process including the localized formation of domains with constrasting higher cross-link density, often referred to as microgels in the literature, and the evolution of the initially isolated particles into a continuous glassy material is lacking. Furthermore, the typical dimensions and physical features of the domains concerned in the different stages of network build-up are subject to speculation.

In a previous work,[12] we used temperature-modulated differential scanning calorimetry (TMDSC) to study aromatic diacrylate networks that exhibit two main overlapping second-order thermodynamic events assigned to the glass transition, clearly evidenced in the differentiated form of the reversing heat capacity signal, $dC_{p,rev}/dT$. The experimental data were quantitatively exploited by means of a two-component model for describing the network by a biphasic-like polymer blend with constituting domains exhibiting physical features varying continuously as the average level of conversion increases. We have proposed a consistent scenario based on the spread in time nucleation and growth of microgels starting at very low monomer conversion that produces a distribution of relaxation temperatures of increasing heterogeneity that corresponds to the various physical states of the microgels. Because of progressive vitrification, all microgels eventually reach a final state with similar cross-link density, inducing some homogeneization of the distribution for conversion levels higher than 0.6. The population of clusters was also found to influence strongly the conditions of the polymerization that proceed in the interstitial domains where a larger number of defects seem to be created as the global conversion increases.

Some questions were nevertheless raised and not addressed. In particular, whereas the partial overlapping of the two main transitions revealed in TMDSC suggests the existence of more-or-less diffuse interphase linking microgels and loosely cross-linked areas; it was not possible to obtain detailed information about its development or to clarify its influence on network build-up. Interesting complements can be brought up by imaging techniques such as electronic microscopies[13] or atomic force microscopy (AFM) that can provide direct visualization of the different structures forming the polymeric networks. In particular,

*Corresponding author. Tel/Fax: 33 3 26 91 33 38. E-mail: xavier.coqueret@univ-reims.fr.

Published on Web 09/15/2010

Scheme 1. Structure of the Studied Diacrylate Monomers

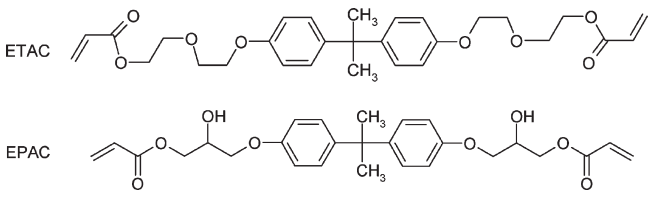

AFM potentially offers nanometric resolution, whereas it is not sensitive to charge effects and is unaffected by weak contrast of stopping power for electrons, which often limits the relevance of scanning electronic microscopy applied to polymer materials.[14,15]

For these reasons and also because of the simplicity of the sample preparation, several authors have selected and implemented AFM for measuring the height profile of various types of ion-etched networks based on vinyl ester resins,[16] unsaturated polyesters,[17] or vinylester/epoxy blends.[18] The obtained pictures revealed the presence of some nodular or worm-like features depending on the system.

In the present investigation, AFM was used in the tapping mode for imaging the film surface by the phase contrast mapping. Whereas the height image corresponds to the vertical displacement necessary to keep constant the oscillating amplitude of the probing tip, the phase image records the phase lag of the oscillator relative to the cantilever response. Phase imaging maps the viscoelastic,[19] adhesion,[20] and stiffness[21] variations in the studied samples in direct relation with the local Young's modulus.[22] This technique has already been used to characterize soft and rigid segments of block copolymers[23] as well as blends of poly(methyl methacrylate) and polybutadiene.[24]

Consequently, we were expecting to visualize the heterogeneities of cross-link density in networks obtained by the radiation−initiated polymerization of two aromatic diacrylates derived from bisphenol A (BPA), an ethoxylated BPA diacrylate named ETAC, and a BPA epoxy diacrylate named EPAC (Scheme 1). The latter exhibits distinct structure and hence distinct physical properties in the liquid monomer state as well as in the cured state, essentially because of the possibility of intermolecular H-bonding in EPAC. The monomers are liquids a room temperature (RT), and they both include a rigid core, ensuring the formation of a network with T_g above RT at low conversion. That feature is particularly convenient for revealing heterogeneities of cross-link density by AFM measurements performed at RT. Also, it is representative of several aromatic acrylate monomers used frequently for high-performance composite materials.

Experimental Section

Material and Polymerization Procedure. Ethoxylated bisphenol A diacrylate (ETAC) from Sartomer (reference SR601E) and bisphenol A epoxy diacrylate (EPAC) from Cytec (reference Ebecryl 600) were used as received, without diluents.

The liquid monomers were cast on NaCl plates using a bar coater for obtaining 20 μm thick films. Photopolymerization was achieved under 365 nm UV irradiation (Philips TL08, 7 mW·cm^{-2}) by exposing the liquid monomer mixed with a limited amount (0.1, 0.5, or 2 wt %) of 2-hydroxy-2-methylpropiophenone (Additol HDMAP, Cytec) so as to avoid any significant light screening effect by the photoinitiator at the working wavelength. Temperature control as well as inerting were achieved using a Linkam hot stage under continuous nitrogen flow. Irradiation time ranged from 30 s to 20 min, whereas the temperature was varied between 25 and 125 °C to obtain acrylate conversion levels ranging from approximately 0.2 to 0.7

Electron beam curing was achieved without any photoinitiator. The 150 keV application development unit from Advanced Electron Beams was used. Nitrogen inerting of the irradiation chamber was achieved for avoiding surface inhibition of free radical polymerization by atmospheric oxygen. The applied dosed was varied from 5 to 400 kGy by increment never exceeding 35 kGy so as to limit excessive temperature rise within the samples. Beam current was typically set to 10 mA, with conveyor speed between 15 and 45 m·min^{-1}. The exposure was repeated to reach the desired dose. A few samples were purposely prepared with a low level of conversion, the beam current being set to 2.5 mA.

Conversion Monitoring. Infrared spectra were directly recorded from the samples cured on the NaCl substrate using a Fourier transform infrared Bruker alpha-T spectrophotomer. The decrease in absorbance at 810 cm^{-1} (−CH=CH$_2$ out of plan deformation) was measured taking into account that the invariant band centered at the reference wavenumber 830 cm^{-1} A^t_{830} (aromatic −CH= deformation) has a contribution to the absorbance A^t_{810} measured at 810 cm^{-1} amounting to 16% of A^t_{830}. The conversion was thus calculated using the following equation

$$\pi = 1 - \frac{A^t_{810} - 0.16A^t_{830}}{A^0_{810} - 0.16A^0_{830}} \quad (1)$$

AFM Observation. AFM analyses of the top surface of the diacrylate films were performed under ambient conditions using a Dimension setup equipped with a Nanoscope V controller from Veeco. A silicon tip with a nominal resonance frequency around 320 kHz, a nominal spring constant around 40 N·m^{-1}, and a nominal tip radius of 5 to 10 nm was used to record height and phase images simultaneously. To obtain information about the stiffness of the surfaces, experiments were performed using hard tapping conditions. In this mode, the ratio of the set-point amplitude to the free-oscillation amplitude is taken between 0.3 and 0.5 to increase the interactions between the tip and the sample. Large oscillation amplitudes were used to avoid a possible effect of the adsorbed water at the sample surface. For such imaging conditions, the interaction between the tip and the sample becomes repulsive, and the contrast in the phase image is related to the variation of the local surface stiffness. For all images, the phase scale was shifted so that the zero-phase signal in black corresponds to soft domains and the positive phase values in white correspond to the stiffest domains. Because the variations of the average sample stiffness were increasing with monomer conversion, the tip oscillation and acquisition parameters were adjusted for optimizing the phase contrast image obtained for each sample in a series. Therefore, the comparison of absolute phase values between the pictures is not relevant. For both reasons, the initial setting for the phase scale was kept unchanged for all reported experiments: close to 0° phase for the relative softest domains appearing in black in the images and maximum positive phase values for the relative stiffest domains appearing in white in the images. Images were recorded at scan rates of 0.5 Hz. All images were processed and treated using WSxM[25] and ImageJ 1.40 g software. If not specified, all images have been denoised using a wavelet filter.[26]

Results and Discussion

AFM Phase Signal and Heterogeneities of Cross-Link Density. Figure 1 represents the height and the phase images recorded from the same area of an EPAC network polymerized under UV radiation to a conversion level of $\pi = 0.40$. The topographical image shows a very flat sample with a root-mean-square (rms) roughness of 0.25 nm, whereas the phase contrast image highlights a more complex and heterogeneous structure. With the experiment conditions used for the present work, tip interactions with stiffer areas induce a positive phase shift, whereas the phase of very compliant domains is close to 0°. The apparent morphology therefore

reveals the presence of stiff domains (whiter zones) corresponding to the higher phase values, whereas the darker zones correspond to much softer materials. The network thus appear as interconnected rigid clusters of characteristic dimension of some tens of nanometers, which form a continuous domain including islands of very soft material.

The stiff domains can be reasonably interpreted with the presence of clusters, originating from the initial microgels, that are readily converted to a densely cross-linked structure contrasting with the softer interstitial zones that likely correspond to the loosely cross-linked and swollen matrix.

Owing to the absence of significant surface roughness in the samples studied in this work, we can conclude that the strong variations of phase correspond to true heterogeneities and that they are not artifacts due to tip scratching on hills or to some decrease in resolution due to deep holes.[27] The forthcoming pictures in this Article will show only phase images. Owing to the adjustments described in the Experimental Section, absolute phase values cannot be quantitatively compared with one sample to another. For the sake of simplicity, the phase scales were therefore omitted.

Microgel Nucleation and Evolution. The set of five images shown in Figure 2 was recorded from EB-cured ETAC networks. Monomer conversion varies from $\pi = 0.31$ to 0.81 for irradiation doses ranging from 5 to 400 kGy, respectively. For the sample with the lowest conversion, the phase image is already heterogeneous with the presence of some small clusters and a few aggregates with slightly higher phase. Nevertheless, the contrast is weaker than that for more converted films. Indeed, in the second sample ($\pi = 0.46$), the phase image has undergone significant changes in terms of contrast. One can observe two distinct types of domains, with interconnected clusters and isolated low phase islands corresponding to smoother domains. For conversions of $\pi = 0.60$ and 0.67, the characteristic dimension of the clusters is larger, and the overall image becomes brighter as the overall conversion increases. Concerning the darker soft domains, it seems that they initially increase in number when conversion is increased from $\pi = 0.31$ to 0.46. Then, they tend to increase both in average size and in number for higher conversion values. The contrast enhancement observed when conversion increases from $\pi = 0.31$ to 0.46 can be interpreted by some phase separation phenomenon. In low conversion systems, the incipient network is swollen by the unreacted monomer, modifying the viscoelastic behavior at the probing frequency. We have conducted swelling experiments with samples made of the aromatic diacrylate ETAC that were converted to macroscopic gels of average conversion $\pi \approx 0.15$. By soaking the samples in the starting monomer, we have measured a 6% weight gain due to monomer swelling into the gel. This observation clearly supports the possibility of monomer transport toward the polymer network domains at low conversion.

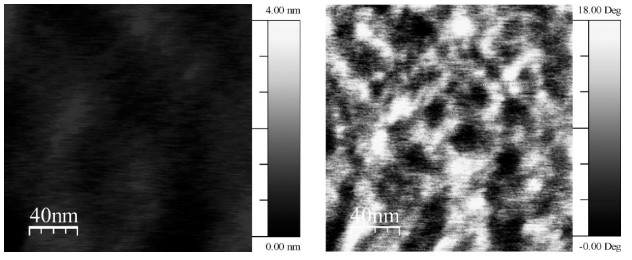

Figure 1. Raw height (left) and phase (right) images (200×200 nm^2 area) of UV-cured EPAC network with a conversion level $\pi = 0.40$ (7 mW·cm^{-2}, 10 min at 50 °C, photoinitiator content: 0.1 wt %).

For higher conversion levels, the miscibility of the monomer in the polymerized network decreases as a consequence of higher cross-link densities, generating monomer-rich areas by phase separation of the unreacted liquid from the swollen scaffold that is submitted to contraction and that finally collapses.[28] Continuation of initiation in the monomer-rich domains thus generates new microgels, soon converted to clusters, with induction of phase separation on a smaller dimension scale. This phenomenon can also explain why darker domains first tend to increase in number before decreasing, whereas their mean size continues to rise.

We have further analyzed the presented images for following the evolution of quantitative geometric descriptors associated with the rigid domains over the investigated conversion range. This was achieved by appropriate binarization and threshold operations of the relative higher phase zones on the denoised images related to a known monomer

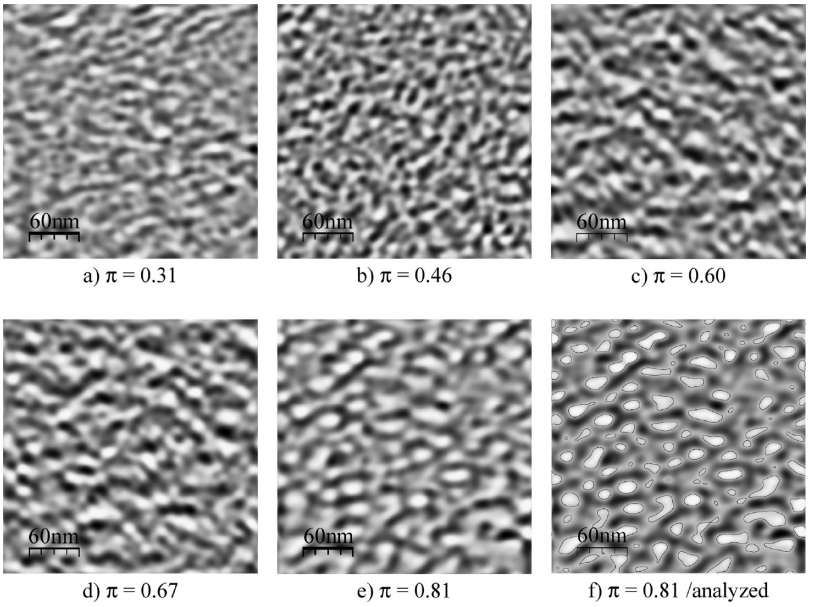

Figure 2. Phase images of EB-cured ETAC networks (300×300 nm^2 area) with conversion ranging from $\pi = 0.31$ to 0.81 for corresponding irradiation doses ranging from 5 to 400 kGy. Image (f) corresponds to image (e) with delimitation of higher phase domains.

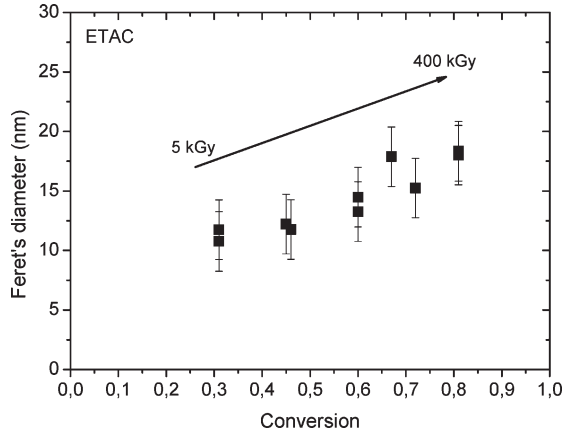

Figure 3. Evolution of the cluster mean Feret's diameter as a function of radiation dose for EB-cured ETAC networks (150 keV electron beam, the radiation dose being varied from 5 to 400 kGy).

conversion. This is illustrated in Figure 2 for the sample converted to a monomer conversion of $\pi = 0.81$, where we have circled the analyzed entities. The two prime descriptors we have considered are Feret's diameter and the area of the rigid clusters. The histogram tool for thresholding the images was used. Indeed, the gray scale histograms reveal that the transition between the rigid zone and the softer surrounding medium is covered only by a small number of steps, suggesting a sharp profile of phase shift between the different domains. This particular feature of the contrast allowed us to achieve image analysis with better reproducibility. The standard error on the mean Ferret's diameter was evaluated to be ~2.5 nm.

The average Feret's diameter measured for the clusters observed in representative 300 × 300 nm^2 images is shown in the plots of Figure 3. The characteristic dimension is increased by a factor 1.73, from 11 to 19 nm, when monomer conversion progresses form $\pi = 0.31$ to 0.81. Assuming an isotropic growth of the domain, this expansion would correspond to an increase in volume by a factor slightly higher than 5.

The Feret's diameter reaches very early a value of ca. 10 nm and then undergoes a moderate evolution, 20 nm being the limiting size for this system. However, the general trend suggests a more important increase when conversion tends to completion. Owing to the change of circularity of the rigid objects, we can suspect that for monomer conversion lower than 0.60, cluster growth is due to swelling and by polymerization occurring at the surface of the nodular clusters involving the pendant unreacted acrylate groups peripheral to the densely cross-linked domains. For conversion levels above this value, because of the vitrification that precludes cluster deformation and permeability, the growth would be essentially caused by aggregation of adjacent clusters by cross polymerization in the contact areas.

On the basis of the observation of images presented in Figure 2 and of mean Feret's diameter variations, one can suppose that cluster aggregation concerns only two or three initially isolated microgels; further aggregation is limited either by the absence of mobility for the particle or because of too large of a gap between neighboring particles.

In an attempt to confirm this hypothesis, we determined the distribution of relative area measured for rigid clusters in the plane images. For each conversion level, the different populations were sorted according to the individual areas into 50 nm^2 broad classes. The corresponding fraction of the

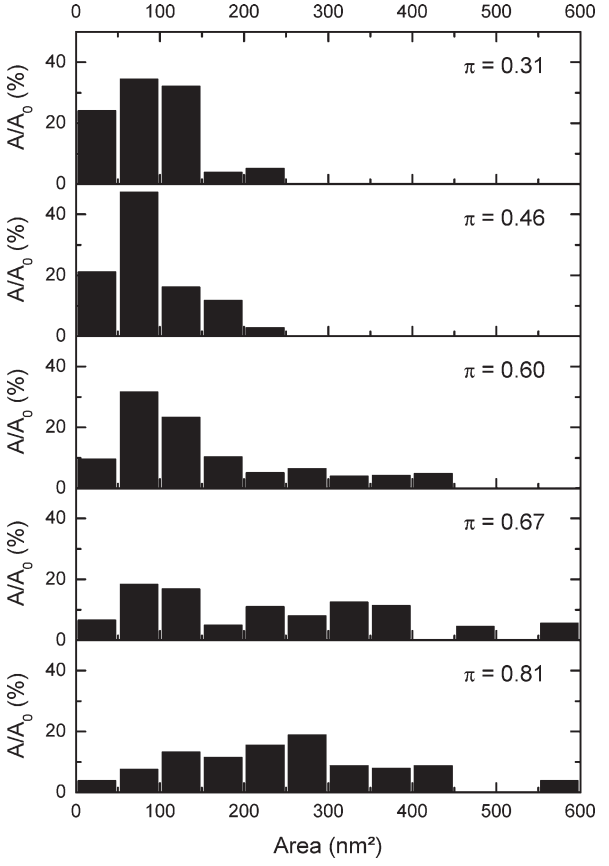

Figure 4. Distribution of the fractional area of clusters relative to the total area of rigid domains for EB-cured ETAC networks polymerized to different conversion levels (150 keV beam).

total area assigned to each population is presented on the histograms of Figure 4. For conversion levels of $\pi = 0.31$ and 0.46, the population of clusters exhibiting an area (A) < 50 nm^2 represents 25% of the overall area covered by the rigid domains. For higher conversions, this value decreases significantly. The contribution of the second class (50 < A < 100 nm^2) increases from 35 to 45% between $\pi = 0.31$ and 0.46. For $\pi = 0.60$, this population begins to decrease, but it is still central in the distribution. This decrease is even more important at higher conversion. Finally, for the population corresponding to the larger areas (A > 100 nm^2), we notice a maximum area of ~250 nm^2 until $\pi = 0.46$, and then for $\pi = 0.60$, we observe a significant increase in the areas with a distribution centered at 250 nm^2 for $\pi = 0.81$. These observations help support a mechanism with clusters nucleating until the conversion level of $\pi = 0.46$ without significant growth in size. For conversions superior or equal to 0.6, the broadening of the area distribution would be the result of aggregation of closed clusters producing some densification of the network. Because no significant increase in size is observed for conversions lower than 0.5, we can exclude the growth of the clusters for higher conversion values when the mobility of reactive species is strongly reduced. Consequently, the domain of intermediate conversion, with π values between 0.46 and 0.60, seems to be a transition zone marking the end of microgel nucleation because of a lack of free space to the benefit of an aggregation process. Moreover, it is also interesting to notice that for $\pi = 0.60$, the distribution is centered on the area value of 100 nm^2, whereas for the conversion level $\pi = 0.81$, the center of the distribution is ~250 nm^2. This tends to support the fact that the aggregation process mainly concerns only two or three initially isolated particles.

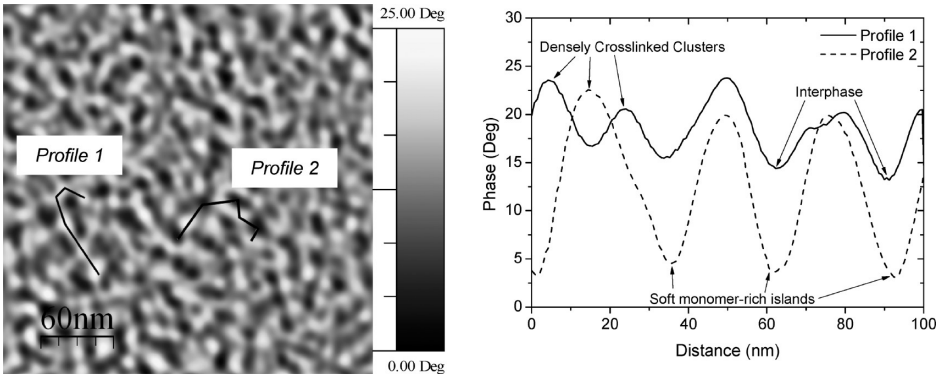

Figure 5. Mapping path and corresponding phase profiles obtained by AFM probing of an EB-cured ETAC network of conversion level $\pi = 0.46$ (150 keV beam, dose = 8 kGy, beam current = 2.5 mA, conveyor speed = 30 m·min^{-1}, 1 pass).

Nevertheless, it must be mentioned that even for conversion as high as $\pi = 0.81$, according to the method described above, significant areas are not counted. Indeed, by imposing a threshold level to 75% of the highest phase, rigid clusters represent 20% of the total area of the image. By lowering the threshold level to 50% of the highest phase, rigid domains contribute to 50% of the surface fraction. Finally, knowing that areas having a phase value lower than 20% of the highest phase contribute to only 4% of the total area, it is clear that significant areas have not been studied and turn out to be constituted by an interphase domain linking rigid clusters and soft islands.

Interphase Development. The AFM investigations presented in the previous section illustrate well the limitations brought by a biphasic-like network structure only considering very stiff domains surrounding by soft regions. Indeed, even for a high conversion level of $\pi = 0.81$, it appears that almost 50% of the image surface fraction is neglected if we apply a threshold level equal to 50% of the highest phase. This suggests the existence of an interphase zone where conversion is higher than the soft islands but lower that the densely cross-linked clusters isolated during the counting operation. Appearing as intermediate phase values on AFM images, this interphase seems to play an important role. Figure 5 illustrates the existence of these intermediate conversion areas by plotting the phase profile according to different directions. Profile 1 shows periodic maxima corresponding to isolated clusters, with phases never reaching 0° values with peak-to-peak amplitude $< 10°$. According to profile 2, the peak-to-peak amplitude is substantially higher, about 15−20°. This means that according to profile 1, the clusters are linked by an intermediate conversion interphase that can be appreciated on the AFM images by a stringy network of intermediate phases. When looking at profile 2, rigid clusters are separated by monomer-rich islands with high phase contrast and consequently high conversion contrast. From a mechanical point of view, we can advance that network structure is given by this wide stringy network including isolated or aggregated clusters, whereas the isolated soft islands are responsible for secondary relaxation that can be observed in dynamic mechanical analysis experiments, for example. This assumption is also supported by the fact that for conversions as low as $\pi = 0.10$ we noticed that the ETAC network forms a macroscopic single object that can be handled, suggesting the existence of a flexible scaffold having sufficient mechanical resistance to the deformations caused by swelling, to self-standing, and to the stress due to handling. This monolithic feature for such low monomer conversion cannot be explained in the case of a network composed of some cross-linked microgels in an essentially unpolymerized matrix. This stringy network could be the missing piece, ensuring to the microgel the mechanical resistance required to form a free-standing soft object. In addition, if we take into account our anterior TMDSC results,[7] then this network would also strongly influence the thermal properties of the whole material, even at slightly higher conversion levels. Indeed, we have shown that for a conversion level as high as 0.8 the high-T_g component evidenced by TMDSC contributed to 65% of the total area under the $dC_{p,rev}/dT$ signal, indicating that approximately a similar fraction of the material is contributing to the high-T_g component. For a sample of similar conversion, AFM observations evidenced that the cluster area would contribute to only 20−50% of the total image areas, depending on selected value for the thresholding level. Such a difference is explained when assuming that the high-T_g component isolated in TMDSC not only concerns rigid clusters but also includes a significant fraction of the network interconnecting them.

All of these observations can now be gathered to substantiate the electron-beam-induced cross-linking polymerization scenario of diacrylate monomers that we tried to illustrate in Figure 6. Starting from the uncured monomer mixture (A), we believe that polymerization effectively proceeds by a process similar to polymerization-induced phase separation and spinodal decomposition. After first initiation events, cross-linking polymerization starts, but because of better intramolecular reactivity, local cyclization and autoacceleration occur to form microgels. Parallel to this, the stringy network begins to establish and because of its affinity with the cross-linked zone will tend to link the nucleating microgels, ensuring for conversion as low as 0.1 or 0.2 a macroscopic monolithic aspect (B). Of course, for such low monomer conversion, the structure is completely swollen by the monomer. As conversion increases, monomer affinity with the polymerized network decreases so that it phase separates outside the microgels and either contributes to densification of the stringy network or, to a lesser extent, contributes to the growth of the microgels if unreacted acrylate groups are accessible (C). For even higher conversion, densely cross-linked clusters will not be able to grow anymore because of a lack of mobility for the reactive species and accessible unreacted functions, and the densification of the stringy network will lead to an even constrained environment. This will lead to the aggregation of some cluster microgels because of network rearrangement, whereas the uncured monomer will be the only species with sufficient mobility to gather in monomer-rich pools because of the respective affinities (D).

Comparison with UV-Curing and with EPAC-Based Networks. In our previous study of the same EB- or UV-cured

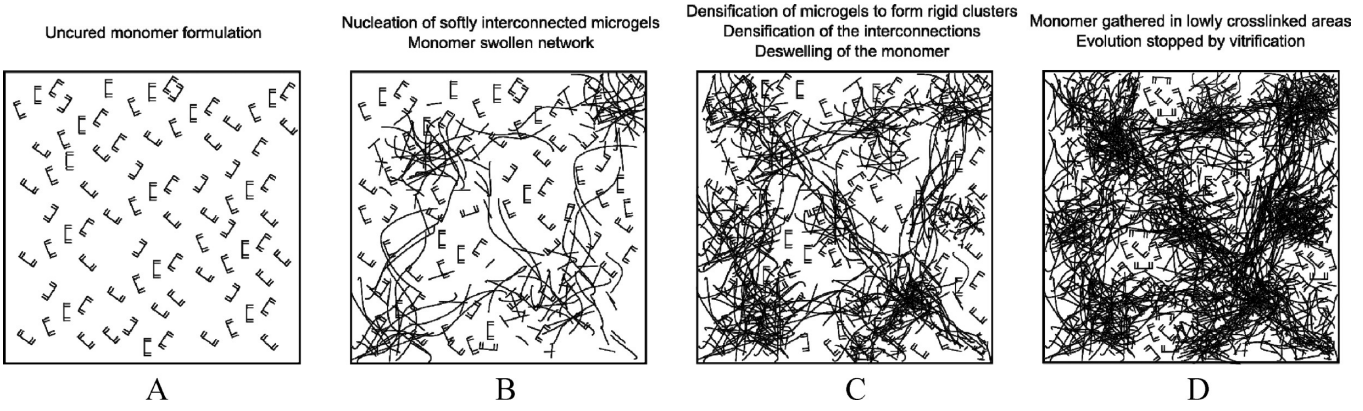

Figure 6. Proposed scenario for the structure development in radiation-cured aromatic diacrylate networks.

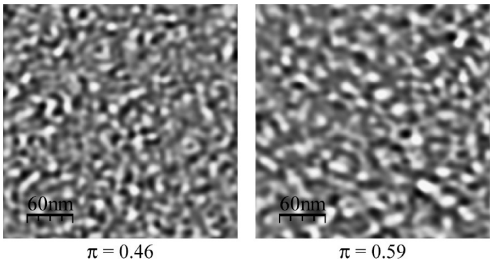

Figure 7. Phase images (300 × 300 nm^2 area) of UV-cured ETAC networks for two conversion levels (7 mW·cm^{-2}, photoinitiator content: 0.1 wt %).

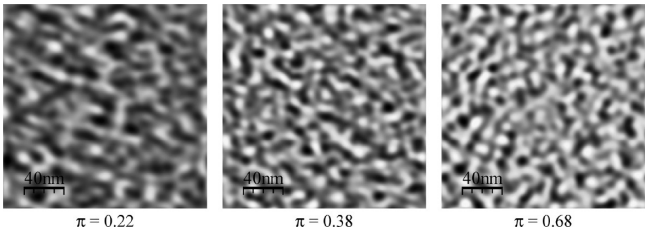

Figure 8. Phase images (200 × 200 nm^2 area) of a set of UV-cured EPAC networks polymerized to various conversion levels (7 mW·cm^{-2}, photoinitiator content: 0.1 wt %).

networks using temperature-modulated differential scanning calorimetry,[7] we have pointed out that the initiation mechanism has no significant influence on the thermal features of the heterogeneous materials. We have also compared using AFM the network structures for the different modes of activation. Figure 7 gives phase images of two UV-cured ETAC networks including 0.1 wt % of photoinitiator with respective conversion levels of $\pi = 0.46$ and 0.59 so that we can compare with their EB-cured equivalents previously presented in Figure 1. The UV-cured samples also present a structure including clusters contrasting well with the surrounding media. Their mean diameter is very close to what we obtained on EB-cured samples. Again, we can evidence the stringy network of intermediate conversion that forms a net, entrapping one or a limited number of clusters; finally, monomer-rich pools are also present, appearing as dark islands. We can conclude that the absence of differences between networks resulting from the two types of initiation mode revealed by macroscopic calorimetric analyses is confirmed on a small dimension scale by the AFM experiments.

Networks obtained from EPAC monomer were also studied for comparison with the ETAC-based materials. Some images obtained from UV-cured samples are given Figure 8. Again, we observe the characteristic features of a population of rigid clusters interconnected by a stringy network of intermediate phases and surrounded by the soft low-phase domains. Within the domain of monomer conversion ranging from $\pi = 0.22$ to 0.68, the clusters do not undergo a significant increase in size, but their number increases. Parallel to that, we can observe a strong densification of the stringy network that also supports the interpretation previously developed in this Article. Compared with the ETAC networks, the limit size of the rigid clusters seems to be here around 15 nm. We can relate the smaller diameter to the viscosity of the uncured monomer. Indeed, at 25 °C, ETAC monomer possesses a viscosity of 925 mPa·s, whereas it is ~80 000 mPas for the EPAC monomer, this difference being mainly due to intermolecular hydrogen interactions. Consequently, monomer diffusion in the starting monomer as well as in the presence of a network is severely decreased in EPAC upon curing. Furthermore, material vitrification occurs at a much lower level of monomer conversion. Both effects can limit the growth of the clusters.

To complete the study of UV-cured systems, we also checked the influence of photoinitiator content on network structure. Figure 9 illustrates this aspect with phase images acquired on photopolymerized EPAC networks including 0.1, 0.5, or 2 wt % of photoinitiator. By comparing the presented images for similar conversion levels, no significant influence can be pointed out with regard to the photoinitiator concentration. Again, the absence of dependence on initiation conditions is consistent with our previous results. Another comment can be made on these images when comparing the two samples including 0.5 wt % of photoinitiator. Indeed, a qualitative analysis of microgel mean size would indicate that microgels are wider for the conversion level of $\pi = 0.43$ than for $\pi = 0.61$. Actually, as already mentioned, comparison of absolute phase between two samples cannot be compared because the differences of stiffness between two samples polymerized to different conversion levels requires different tip oscillating parameters.

Nevertheless, quantitative analysis of the relatively higher phase domains for each sample ends effectively in a larger mean Feret's diameter for the sample having the higher conversion level. This difference between naked eye appreciation and quantitative analysis is explained by the presence of low and intermediate conversions of the uncured monomer that swells the microgels and leads to the presence of wide diffuse domains of relative high mean phases that are misleading upon direct observation of the images. This is not the case for the high monomer conversion levels where uncured monomer is essentially gathered in monomer-rich pools.

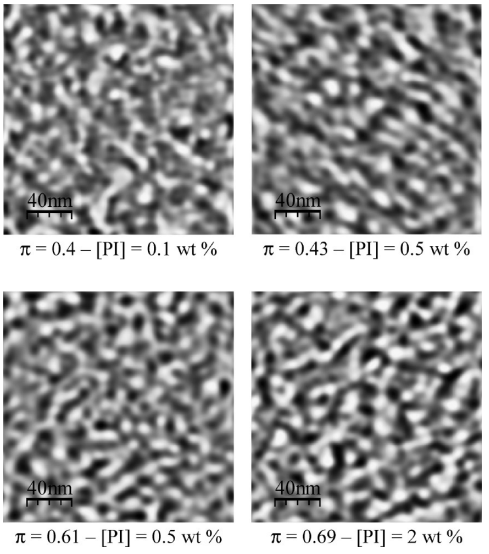

Figure 9. Phase images (200 × 200 nm^2 area) of UV-cured EPAC networks including different amounts of photoinitiator.

Conclusions

Phase imaging using atomic force microscopy in the tapping mode is demonstrated as a convenient technique for mapping the viscoelastic heterogeneities of radiation-cured aromatic diacrylate networks. Rigid clusters having a typical dimension of 15 nm were evidenced from the early steps of the curing process. The evolution of the relative importance of hard and soft domains was quantified as a function of radiation dose for samples covering a broad range of conversion.

Whereas our previous investigation by TMDSC suggested that a two-component model satisfactorily depicted the heterogeneities of radiation-cured ETAC and EPAC networks, we have found that three basic domains with distinct elasticity are required to describe the evolution of the materials microstructure. Rigid nodules exhibiting a mean characteristic dimension of ~15 nm were observed very early in the cross-linking polymerization process. Those clusters initially embedded in a soft gel undergo limited evolution by growth and by aggregation up to a limiting size at higher conversion levels. Nucleation within the monomer-rich domains further continues up to ca. 50% conversion, together with limited growth by aggregation of adjacent particles. Polymerization then continues in interstitial domains, generating a stringy network with some isolated low conversion domains. ETAC and EPAC networks were found to undergo the same network build-up process. Additionally, there was no significant difference in morphology between samples obtained by EB- or UV-induced polymerization or the selected aromatic diacrylates.

Acknowledgment. We express our gratitude to Dr. B. Defoort and Dr. G. Larnac (Astrium Space Transportation) for their support of our studies on radiation-induced polymerization. Financial support by Conseil Regional Champagne Ardenne, MENESR, and EU-FEDER Programme (CPER Project PlAneT) and by the EADS Foundation is gratefully acknowledged.

References and Notes

(1) Bowman, C. N.; Kloxin, C. J. *AIChE J.* **2008**, *54*, 2775–2795.
(2) Dusek, K.; Galina, H.; Mikes, J. *Polym. Bull.* **1980**, *3*, 19–25.
(3) Decker, C. *Prog. Polym. Sci.* **1996**, *21*, 593–650.
(4) Dusek, K. *Polym. Prepr.* **1970**, *11*, 536–540.
(5) Korolev, G. V. *Russ. Chem. Rev.* **2003**, *72*, 197–216.
(6) Wen, M.; Scriven, L. E.; McCormick, A. V. *Macromolecules* **2003**, *36*, 4140–4150.
(7) Kloosterboer, J. G. *Adv. Polym. Sci.* **1988**, *84*, 1–61.
(8) Kannurpatti, A. R.; Anderson, K. J.; Anseth, J. W.; Bowman, C. N. *J. Polym. Sci., Part B: Polym. Phys.* **1997**, *35*, 2297–2307.
(9) Guo, Z.; Sautereau, H.; Kranbuehl, D. E. *Macromolecules* **2005**, *38*, 7992–7999.
(10) Anseth, K. S.; Bowman, C. N. *Chem. Eng. Sci.* **1994**, *49*, 2207–2217.
(11) Wen, M.; Scriven, L. E.; McCormick, A. V. *Macromolecules* **2003**, *36*, 4140–4150.
(12) Krzeminski, M.; Molinari, M.; Troyon, M.; Coqueret, X. *Macromolecules* **2010**, *43*, 3757–3763.
(13) Anseth, K. S.; Bowman, C. N. *J. Polym. Sci, Part B: Polym. Phys.* **1995**, *33*, 1769–1780.
(14) van den Berg, R.; de Groot, H.; van Dijk, M.; Denley, D. *Polymer* **1994**, *35*, 5778–5781.
(15) Jagtap, R. N.; Ambre, A. H. *J. Polym. Mater.* **2005**, *21*, 1–26.
(16) Rey, L.; Duchet, J.; Galy, J.; Sautereau, H.; Vouagner, D.; Carrion, L. *Polymer* **2002**, *43*, 4375–4384.
(17) Mosiewicki, M. A.; Schroeder, W. F.; Leite, F. L.; Hermann, P. S. P.; Curvelo, A. A. S.; Aranguren, M. I.; Borrajo, J. *J. Mater. Sci.* **2006**, *41*, 6154–6158.
(18) Karger-Kocsis, J.; Gryshchuk, O. *J. Appl. Polym. Sci.* **2006**, *100*, 4012–4022.
(19) Tamayo, A.; Gracia, R. *Langmuir* **1996**, *12*, 4430–4435.
(20) Schmitz, I.; Schreiner, M.; Friedbacher, G.; Grasserbauer, M. *Appl. Surf. Sci.* **1997**, *115*, 190–198.
(21) Magonov, S. M.; Elings, V.; Whangbo, M.-H. *Surf. Sci.* **1997**, *375*, L385–L391.
(22) Godehart, R.; Lebek, W.; Adhikari, R.; Rosenthal, M.; Martin, C.; Frangov, S.; Michler, G. H. *Eur. Polym. J.* **2004**, *40*, 917–926.
(23) McLean, R. S.; Sauer, B. B. *Macromolecules* **1997**, *30*, 8314–8317.
(24) Raghavan, D.; VanLandingham, M.; Gu, X.; Nguyen, T. *Langmuir* **2000**, *16*, 9448–9459.
(25) Horcas, I.; Fernández, R.; Gómez-Rodríguez, J. M.; Colchero, J.; Gómez-Herrero, J.; Baro, A. M. *Rev. Sci. Instrum.* **2007**, *78*, 013705.
(26) Gackenheimer, C.; Cayon, L.; Reifenberger, R. *Ultramicroscopy* **2006**, *106*, 389–397.
(27) Bar, G.; Thomann, Y.; Brandsch, R.; Cantow, H.-J.; Whangbo, M.-H. *Langmuir* **1997**, *13*, 3807–3812.
(28) Anseth, K. S.; Anderson, K. J.; Bowman, C. N. *Macromol. Chem. Phys.* **1996**, *191*, 833–848.